

# **Evolution of orientation distributions of $\gamma$ and $\gamma'$ phases during creep deformation of Ni-base single crystal superalloys**

Toru Inoue<sup>1</sup>, Katsushi Tanaka<sup>1†</sup>, Hiroki Adachi<sup>1</sup>, Kyosuke Kishida<sup>1</sup>, Norihiko L. Okamoto<sup>1</sup>, Haruyuki Inui<sup>1</sup>, Tadaharu Yokokawa<sup>2</sup> and Hiroshi Harada<sup>2</sup>

<sup>1</sup>Department of Materials Science and Engineering, Kyoto University, Sakyo-ku Kyoto 606-8501, Japan and <sup>2</sup>National Institute for Materials Science, Tsukuba 305-0047, Japan

## Abstract

The evolution of orientation distributions of  $\gamma$  and  $\gamma'$  phases in crept Ni-base single crystal superalloys have been investigated by theoretical calculations with elastic-plastic models and by experiments. As creep deformation proceeds, the crystallographic orientation distributions for both phases are broadened as a result of the waving of the raft structure, which occurs to reduce the total mechanical energy. The broadening of the orientation distribution occurs in such a way that the 001 pole broadens isotropically while the  $hk0$  poles broaden preferentially along  $\langle 001 \rangle$  directions. Since the extent of the broadening increases almost linearly with the amount of creep deformation, the measurement of the broadening by X-ray diffraction can be utilized in non-destructive methods to predict the lifetime of Ni-base superalloys.

## 1. Introduction

Nickel base single crystal superalloys exhibit superior high temperature creep strength and oxidation resistance, and have been applied to turbine blades in industrial gas turbines and aero engines. The creep strength of superalloys has been known to be closely related to the microstructure. After appropriate heat treatments, superalloys exhibit a microstructure frequently referred to as cuboidal structure, where the cuboidal  $L1_2$ -ordered  $\gamma'$  phase coherently precipitates in the fcc (face centered cubic) disordered  $\gamma$  phase matrix and forms a simple cubic array along the three principle axes of the cubic crystal structures. When modern superalloys are subjected to creep deformation with a

---

<sup>†</sup> To whom all correspondence should be addressed.

relatively low tensile stress along [001] at high temperatures, the  $\gamma'$  precipitates are coarsened preferentially in the (001) plane to form a lamellar structure, which is usually called a raft structure, where  $\gamma$  and  $\gamma'$  plates expanding in the (001) plane stack alternately. Since the dislocation motion is hindered by lateral  $\gamma/\gamma'$  lamellar interfaces, creep deformation is suppressed significantly by the formation of the microstructure [1,2]. Under the influence of the applied stress, the lamellar interfaces in the raft structure gradually deviate from the (001) plane so as to form a wavy raft structure with the amplitude of the wave increases gradually as creep deformation proceeds [3,4]. The waving is known to be driven by the elastic instability of the planar (001) raft structure originated from the elastic field of creep dislocations accumulated at  $\gamma/\gamma'$  interfaces [4,5]. Since the evolution of microstructures affects internal stress/strain states developed during creep deformation and vice versa, knowledge about their mutual relationship is indispensable for understanding creep deformation of Ni-base single crystal superalloys.

Since a characteristic microstructure evolution involving the formation of the raft structure and its waving occurs during creep deformation at high temperatures, the life time prediction for Ni-base single crystal superalloys may be possible by extracting some characteristic changes in microstructural parameters. Some non-destructive methods have indeed been proposed for this purpose. One of the proposed methods is to measure the changes in lattice misfit values between  $\gamma$  and  $\gamma'$  phases by X-ray diffraction [4,6-13]. However, this method seems not to be so useful for the lifetime prediction, since the extent of lattice misfit significantly changes during the first stage of creep where the raft structure is formed, while the lattice misfit value is virtually constant from the beginning of the second stage of creep [4]. The waving of the raft structure that proceeds with creep deformation is expected to be characterized with the increase in the inclined angle of the lamellar interfaces from (001). The distribution of the inclined angle, which corresponds to the variation in local plastic strains introduced during creep deformation, is expected also to increase with the increase in the inclined angle, i.e., with the increase in the amount of creep deformation. Then, the measurement of the orientation distributions of  $\gamma$  and  $\gamma'$  phases by X-ray diffraction is expected to be utilized in non-destructive methods to predict the lifetime of Ni-base superalloys.

In the present paper, we investigate the evolution of orientation distributions of

$\gamma$  and  $\gamma'$  phases in crept Ni-base single crystal superalloys by theoretical calculations with elastic-plastic models and by experiments, in order to establish the mutual relationship between the evolution of microstructures and the development of internal stress/strain states during creep deformation. We also investigate whether the measurement of the broadening of orientation distributions of  $\gamma$  and  $\gamma'$  phases by X-ray diffraction can be utilized as a non-destructive method to predict the lifetime of Ni-base superalloys.

## 2. Method of calculations

### 2.1 Internal stress/strain and elastic energy

We have employed two microstructural models for the elastic-plastic calculations. One is a wavy lamellar model and the other is an inclined lamellar model (Fig. 1). The former is a relatively realistic model, which is defined by two parameters of the waving; the angle between the direction of the wave and the [100] direction,  $\theta$ , and the maximum angle of lamellar inclination,  $\chi$ . This model has been applied to evaluate the stability of the wavy raft structure and the local elastic stress/strain states within the structure. The latter is a simplified model corresponding to some local part of the wavy lamellar model, and this model is defined by the angle between the direction of the wave and the [100] direction,  $\theta$ , and the angle between the normal of the lamellar interface and the [001] direction,  $\phi$ . The inclined lamellar model is applied to evaluate the amounts of creep dislocations introduced and accumulated at  $\gamma/\gamma'$  interfaces.

The microstructural evolution without chemical composition changes is determined by the change in the total mechanical energy. The total mechanical energy corresponding to the Gibb's free energy of the system,  $U$ , is expressed as

$$U = U_{\text{int}} + U_{\text{ext}} + U_{\text{pot}}, \quad (1)$$

where  $U_{\text{int}}$ ,  $U_{\text{ext}}$  and  $U_{\text{pot}}$  are the internal elastic energy, elastic energy caused by the application of an external stress and the potential energy of an external stress, respectively. In the following calculations, we assume that the elastic constants of the  $\gamma$  and  $\gamma'$  phases are identical with each other. On the assumption, only  $U_{\text{int}}$  is affected by the morphology of the microstructure. In other words, the internal energy is not affected by external stresses and/or strains [14,15].

From the reported results of experiments and theoretical calculations, creep dislocations in modern superalloys are considered to move only in  $\gamma$  channels perpendicular to the applied stress but not to pass through  $\gamma$  channels parallel to the applied stress and  $\gamma'$  precipitates under a typical tensile creep condition, for example, at 1373K under 137 MPa [16-18]. As a consequence, only (or mainly) the  $\gamma$  phase is plastically deformed by the motion of creep dislocations. Furthermore, creep dislocations are almost homogeneously introduced in the lateral  $\gamma$  channels [19-21]. With these knowledge, we have introduced the “effective eigenstrain” of the  $\gamma$  phase,  $\boldsymbol{\varepsilon}^*$ , which is a liner combination of the lattice misfit between  $\gamma$  and  $\gamma'$  phases,  $\boldsymbol{\varepsilon}_0$ , and the amount of plastic strain caused by the introduction of creep deformations,  $\boldsymbol{\varepsilon}_p$ , [5]. The former is defined as  $\boldsymbol{\varepsilon}_0 = (a_\gamma - a_{\gamma'}) / a_{\gamma'}$  where  $a$  denotes the lattice parameter. Then, the effective eigen strain in the  $\gamma$  phase with a certain amount of creep dislocations is defined as,

$$\boldsymbol{\varepsilon}^* = \begin{pmatrix} \varepsilon_0 & 0 & 0 \\ 0 & \varepsilon_0 & 0 \\ 0 & 0 & \varepsilon_0 \end{pmatrix} + \boldsymbol{\varepsilon}_p^*, \quad \boldsymbol{\varepsilon}_p^* = d^1 \boldsymbol{\varepsilon}_{(111)[\bar{1}01]}^* + d^2 \boldsymbol{\varepsilon}_{(\bar{1}\bar{1}1)[101]}^* + \dots \quad (2)$$

where  $d^i$  is the amount of creep dislocations belonging to the  $i$ -th slip system and  $\boldsymbol{\varepsilon}_{(111)[\bar{1}01]}^*$  etc. are the corresponding deformation matrices defined as,

$$\{\boldsymbol{\varepsilon}_{\boldsymbol{n}\boldsymbol{b},ij}^*\} = \{n_i b_j\} \quad (3)$$

where  $\boldsymbol{n}$  and  $\boldsymbol{b}$  are slip plane normal and the Burgers vector of the dislocation, respectively [22].

The internal elastic strain field for a given effective eigen strain has been calculated by means of the Fourier-transformation method proposed by Khachaturyan [23], in which the elastic strain at position  $\boldsymbol{r}$ ,  $\boldsymbol{\varepsilon}(\boldsymbol{r})$ , is calculated as

$$\varepsilon_{mn}(\boldsymbol{r}) = \frac{1}{2} \int_{-\infty}^{\infty} \left\{ C_{ijkl} \bar{\xi}_l (G_{im}^{-1} \bar{\xi}_n + G_{in}^{-1} \bar{\xi}_m) \hat{\varepsilon}_{kl}^*(\boldsymbol{\xi}) - \hat{\varepsilon}_{mn}^*(\boldsymbol{\xi}) \right\} \exp(i\boldsymbol{\xi} \cdot \boldsymbol{r}) d\boldsymbol{\xi}, \quad (4)$$

where  $C_{ijkl}$  is the elastic stiffness constants,  $\hat{\varepsilon}_{kl}^*(\boldsymbol{\xi})$  is the Fourier-transformed effective eigenstrain and  $G_{im}$  is the Green's function given by

$$G_{im} = C_{ipmq} \bar{\xi}_p \bar{\xi}_q, \text{ where } \bar{\xi} \text{ is the unit vector parallel to } \boldsymbol{\xi}. \quad (5)$$

The internal elastic stress,  $\sigma_{ij}$ , and energy,  $U_{\text{int}}$ , are respectively given by

$$\sigma_{ij} = C_{ijkl} \varepsilon_{kl} \quad \text{and} \quad U_{\text{int}} = \frac{1}{2} \sigma_{ij} \varepsilon_{ij} \quad (6)$$

The parameters used are reference to the experimental data of the TMS-26 alloy. The lattice mismatch,  $\varepsilon_0$ , is set to be 0.2%, and the elastic constants are  $C_{11}=210$ ,  $C_{12}=150$  and  $C_{44}=95$  GPa, respectively, which were experimentally measured at 1373K [24]. The volume fraction of the  $\gamma$  phase,  $f_\gamma$ , is set to be 7/16, referring to the value experimentally determined from SEM micrographs.

## 2.2 Amount of creep dislocations introduced

To evaluate the amount of creep dislocations introduced for each slip system in the  $\gamma$  phase, we have assumed that the change in the amount of creep dislocations per unit time is proportional to the driving force for the motion of creep dislocations. In general, the Peatch-Koehler force applied to the dislocation is considered as the driving force. On the assumption, the rate equation is expressed as,

$$\frac{\partial d^i(t)}{\partial t} = \alpha \sigma_{pq}(t) n_p^i b_q^i \quad (7)$$

where  $\sigma$  is the calculated elastic stress field and  $\alpha$  is the mobility of dislocations and the superscript  $i$  designates the  $i$ -th slip system. If the time scale is ignored, the value of  $\alpha$  loses its physical meaning and does not affect to the results. We set the value of  $\alpha$  to be  $0.01/|b|$  for the calculations to obtain a convergence in most cases. The amount of creep dislocations can be obtained by solving equation (7) with an iterative calculation.

Since creep dislocations pass thorough narrow  $\gamma$  channels, the driving force for their motion has to be larger than the Orowan stress [19], which is calculated as

$$\tau_c = \frac{\mu b}{\sqrt{3/2}h} \approx 20\text{MPa} \quad (8)$$

where  $\mu$  and  $h$  are shear modulus along the  $\langle 110 \rangle$  direction on the  $\{111\}$  plane (49.1 GPa) and the width of  $\gamma$  channels ( $0.5\mu\text{m}$ ). When the Orowan stress is taken into account, equation (7) is modified as,

$$\frac{\partial d^i(t)}{\partial t} = \alpha |b^i| \left( \sigma_{pq}(t) n_p^i \frac{b_q^i}{|b^i|} - \tau_c \right) \quad (7')$$

### 3. Experimental procedure

#### 3.1 Sample preparation

The samples used are the TMS-26 alloy whose nominal chemical composition is tabulated in Table 1. After a usual heat treatment, the samples were subjected to tensile creep tests along the [001] direction at 1373 K for 0, 0.75, 4, 160, 320 and 360 (ruptured) hours. The crept specimens were cut into thin plates with their faces parallel to the {100} crystallographic plane. The surfaces of the specimens were mechanically polished with colloidal silica for scanning electron microscope (SEM) observations. The specimens for X-ray measurements were mechanically thinned to about the thickness of 0.1 mm, followed by chemical polishing to remove surface damaged layers.

#### 3.2 Measurements of crystallographic orientation distributions

The crystallographic orientation distribution is measured by electron backscattered diffraction (EBSD) combined with energy dispersion X-ray spectrum (EDX) analysis in a SEM and X-ray diffraction (XRD) measurements. The former was used to measure a local deviation of the crystallographic orientation, while the latter to measure the orientation distribution in a relatively large area. The crystallographic orientation distributions of the  $\gamma$  and  $\gamma'$  phases were measured separately utilizing Co map imaging in EDX-EBSD analysis and superlattice diffractions in XRD analysis, respectively.

The geometry of the X-ray measurement is schematically illustrated in Fig. 2. The X-ray radiation of Ag-K $\alpha$  (wave length 0.0567nm) was monochromatized and paralleled by using 111-Si reflection. The radiation was collimated to 0.3 mm in diameter. The rocking curve was measured by rotating the specimen about the  $\omega$  axis with a fixed  $2\theta$  angle set to detect a suitable diffraction. The indices of the diffractions used in the experiment were 400 and 004 ( $\gamma$  and  $\gamma'$ ), and 300 and 003 ( $\gamma'$ ). The resolution of our measurement system is sufficiently high, since the peak width of the rocking curve of Si 400 was about  $0.013^\circ$ , which is by far smaller than those for Ni-base crept specimens of about  $0.2^\circ$ . Since the TMS-26 alloy contains sub-grain boundaries, the measured rocking curves sometimes exhibit several anomalously wide peaks. In order to avoid possible artifacts arising from sub-grain boundaries, several different areas were examined for each specimen.

## 4. Results

### 4.1 Variation of elastic energy calculated with the wavy lamellar model

We have calculated the elastic strain energies with wavy lamellar interfaces in order to examine the stability of the wavy raft structures. In this calculation, we assume that all slip systems operate equivalently, so that  $d^1 = d^2 = d^3 = \dots$  in equation (2). With this assumption, the eigen strain has the tetragonal symmetry. Values of elastic strain energy are shown in Fig. 3 as a function of maximum angle of lamellar inclination in the wavy lamellar model. In the calculation, the creep strain of the  $\gamma$  phase is set to be 0.7%, which corresponds to the strain at the beginning of the second stage of creep for the TMS-26 alloy. The elastic strain energy reaches maximum at the inclination angle of about  $2.5^\circ$  and then decreases with the increase in the inclination angle, i.e., with the increase in the amplitude of the waving. Since the average inclination angle of the lamellar interface from (001) is  $10^\circ$  at the beginning of secondary creep (for about 4 hours), the result of calculation indicates that most lamellar interfaces are elastically unstable in secondary creep so that the amplitude of the wave (i.e., the angle of lamellar inclination) increases spontaneously. This agrees well with the reported experimental results [25].

Stress tensors are calculated at some typical points A-C in the  $\gamma$  phase of a wavy lamellar structure (Fig. 4) under an applied tensile stress of 137 MPa along the [001] direction. At the point A, where the lamellar interface is parallel to (001), all the three diagonal elements of the stress tensor have similar values and the symmetry of the internal stress field is almost tetragonal. Since the hydrostatic stress component cannot be converted into the driving force to move creep dislocations with Burgers vectors of the  $1/2\langle 101 \rangle$ -types, the driving force for the dislocation motion is quite small at the point A. In addition, the elastic stress with a tetragonal symmetry leads to the identical driving force for dislocations with all possible Burgers vectors of the  $1/2\langle 101 \rangle$ -types, maintaining the tetragonal symmetry of the effective eigen strain and elastic stress field. On the other hand, at the points B and C, where the lamellar interface is inclined from (001), the symmetry of the internal stress field is neither hydrostatic nor tetragonal. The symmetry of the stress field is lowered as the inclination angle increases. When the

symmetry of the elastic stress fields is low, the driving forces for the motion of creep dislocations varies from slip system to slip system, leading to the further lowering of the effective eigen strain and of stress.

#### 4.2 Amount of creep dislocations calculated with the inclined lamellar model

The time evolution of the amounts of creep dislocations has been calculated for various lamellar inclination angles, according to the equations (7) and (7'). The results of the calculation are shown in Fig. 5 as a function of iteration step, together with the driving force for the motion of the corresponding dislocations. When the lamellar interface is parallel to (001) (Fig. 5(a)), the driving forces are all identical for the possible 8 slip systems. This indicates that the amount of dislocations accumulated at the lamellar interface is also identical for all the possible 8 slip systems, in accordance with the calculation result with the wavy lamellar model shown in the previous section. In this case, creep dislocations gradually lose their driving force as they move until they stop completely suppressing creep deformation. On the other hand, when the lamellar interface is inclined from (001) (Fig. 5(b)), the amount of creep dislocations introduced in the  $\gamma$  phase differs from slip system to slip system due to the lower symmetry of the stress field. In this case, however, the driving forces for the motion of creep dislocations never diminish to zero, contributing to creep deformation. The driving force for the motion of creep dislocations tends to increase with the increase in the inclination angle. When the Orowan stress is taken into account, creep deformation can be (Fig. 5(c)) or cannot be (Fig. 5(d)) stopped depending on the lamellar inclination angle. There should obviously be the critical inclination angle at which creep deformation cannot be stopped.

The amount of creep dislocations introduced is about  $8 \times 10^6 \text{ m}^{-2}$  for each slip system. This value does not significantly vary with the inclination angle (Fig. 5). This value corresponds to a dislocation network lying on the  $\gamma/\gamma'$  interface with the spacing of about 30 nm. If the dislocation reaction of  $1/2 \langle 101 \rangle + 1/2 \langle 01\bar{1} \rangle \rightarrow 1/2 \langle 110 \rangle$  occurs at the  $\gamma/\gamma'$  interface, the spacing becomes doubled ( $\sim 60$  nm), which value coincides well with the experimentally observed dislocation spacing in a superalloy with the lattice misfit of about 0.2% [21].



#### 4.3 Local crystallographic misorientation analyzed by EDX-EBSD

For local crystallographic misorientation analysis, the ruptured sample was used because a large misorientation between  $\gamma$  and  $\gamma'$  phases is expected to occur. An Cr-map image observed along the [100] direction is shown in Fig. 6(a), in which lighter and darker areas correspond to  $\gamma$  and  $\gamma'$  phases, respectively. Relative values of misorientation examined along a line are plotted in Fig. 6(b). Misorientation within each of  $\gamma$  and  $\gamma'$  lamellae is small, but it occurs at  $\gamma/\gamma'$  interfaces, indicating that the misorientation is originated from creep dislocations accumulated at the  $\gamma/\gamma'$  interface. The extent of misorientation varies from interface to interface, and the averaged value in this case is about  $0.15^\circ$ . The distribution of relative misorientation angles with respect to the averaged orientation examined at points of  $\gamma$  or  $\gamma'$  phases is plotted in Fig. 6(c). The distribution of crystallographic orientations is obviously larger for the  $\gamma$  phase than for the  $\gamma'$  phase, indicating that crystallographic rotation occurs mainly in the  $\gamma$  phase.

#### 4.4 Crystallographic orientation distributions determined by X-ray diffraction

The distributions of crystallographic orientations are also examined by X-ray diffraction through measurements of the full width at half maximum (FWHM) of rocking curves. The variation of FWHMs of 400, 004, 300 and 003 diffractions in the locking curves with creep strain is depicted in Fig. 7. The values of FWHMs for 003 and 004 diffractions increase almost linearly with the increase in the creep strain. The increase in the FWHM value is larger for 004 diffraction ( $\gamma+\gamma'$  phases) than for 003 diffraction ( $\gamma'$  phase), in accordance with the result of the EDX-EBSD analysis. On the other hand, the values of FWHMs for 300 and 400 diffractions are both smaller than are those for 003 and 004 diffractions and are virtually constant from the beginning of secondary creep.

### 5. Discussion

#### 5.1 The stability of the raft structure

We have reported that the raft structure with the lamellar interface parallel to (001) (001 raft structure) is elastically unstable in the stage of secondary creep [5]. The present calculation indicates that the potential to suppress creep deformation through

preventing the dislocation motion varies significantly with the microstructure. When the inclination angle of lamellar interface increases or the Orowan stress decreases by the coarsening of the microstructure, the raft structure loses its potential to suppress further creep deformation. This corresponds to the commencement of tertiary creep. The critical lamellar inclination angle is estimated to be smaller than  $20^\circ$  (Fig. 5(d)). However, the HWHM value observed in the stage of secondary creep corresponds to the inclination angle of about  $20^\circ$ , indicating that there are many lamellar interfaces inclined more than the critical angle even in the stage of secondary creep. This may arise from the fact that the inclined model employed for the calculation of the critical angle is too simplified. Real raft structures consist of many regions having different inclined angles and directions. Long range elastic interactions among these regions decrease the deviation of the elastic stress state from the tetragonal symmetry, which stabilizes the inclined raft structure. The calculations with large scale models that consist of the many regions are required to fill up the discrepancy.

## 5.2 Crystallographic orientation distribution

The waving of the lamellar interface affects significantly the symmetry of the stress fields in the  $\gamma$  phase (Fig. 4) and thereby the amount of creep dislocations accumulated at the  $\gamma/\gamma'$  interface (Fig. 5). In general, crystallographic rotation is caused by dislocations passing through the crystal. The axis of crystallographic rotation is decided by the geometry of the slip system, and the magnitude of rotation is proportional to the amount of dislocations passed through the crystal. If only the  $\gamma$  phase deforms in superalloys, crystallographic rotation of the  $\gamma$  phase is restricted by the undeformed  $\gamma'$  phase. If there is no restriction, the  $\gamma$  phase deforms freely as shown in Fig. 8(a). When the restriction along the  $[001]$  direction caused by the  $\gamma'$  phase is taken into account, the  $\gamma$  phase is rotated about the line vector of dislocations, as shown in Fig. 8(b). Note that the screw component of the dislocations does not affect the crystallographic rotation, if there is no restriction for deformation along the  $[100]$  and  $[010]$  directions.

The crystallographic rotation axis and the rotating direction of the  $\gamma$  phase is tabulated in Table 2, where the directions of (+) and (-) mean a right-handed and left-handed rotations, respectively. The total rotation matrix of the  $\gamma$  phase,  $\mathbf{R}$ , with a set

of the amount of dislocations  $\{d^i\}$  is described as,

$$\mathbf{R} = \begin{pmatrix} 0 & 0 & A+B \\ 0 & 0 & A-B \\ -(A+B) & -(A-B) & 0 \end{pmatrix}, \quad (8)$$

where  $A = -d^1 + d^3 - d^5 + d^7$  and  $B = -d^2 + d^4 - d^6 + d^8$ , respectively. The rotation axis of this rotation matrix is  $(A-B, \overline{A+B}, 0)$ .

Obviously, the  $\gamma$  phase does not rotate when the amount of creep dislocations of all slip systems have the same value. The rotation of the  $\gamma$  phase is caused by the inclination of  $\gamma/\gamma'$  boundaries, which leads to the lowering of the symmetry of stress field in the  $\gamma$  phase, resulting in different amounts of creep dislocations introduced depending on slip system. Since the inclination angle of the lamellar interface and the inclined direction vary from place to place, the observed crystallographic orientation spreads at around the original direction. With equation (8), the distribution of crystallographic orientations of the  $\gamma$  phase with respect to that of  $\gamma'$  phase is estimated and is schematically illustrated in Fig. 9. The broadening of the [001] pole occurs in an isotropic way around the original direction (Fig. 9(b)), but that of the [100] pole occurs in an anisotropic way preferentially along the [001] direction (Fig. 9(c)).

The estimation of the distribution of crystallographic orientations of the  $\gamma$  phase with equation (8) has verified the reason why the rocking curves of 00 $l$  diffractions are broader than those of  $h00$  diffractions in the present measurement, in which X-ray scanning was made along the  $\omega$  direction (Fig. 9(a)). In order to confirm the anisotropic broadening of  $h00$  diffractions (Fig. 9), an additional X-ray measurement with scanning along the  $\chi$  direction (indicated in Fig. 9(a)) was carried out with a (001) slice of the sample crept for 160 h and the result obtained is shown in Fig. 10. When scanning was made along the  $\chi$  direction, the rocking curve of 400 diffraction is almost the same as that of 004 diffraction, in accordance with the above theoretical estimation.

The broadening of crystallographic orientation distributions of  $\gamma$  and  $\gamma'$  phases is now evident to occur as a result of the inequality in the number of introduced dislocations for possible slip systems, which is caused by the inclination of the lamellar interface. Since we can measure the crystallographic orientation distributions in a non-destructive way, for example, by X-ray diffraction, microstructure evolution during

creep deformation, such as how significantly the waving of the lamellar interface occurs, can be readily known through the X-ray diffraction analysis. Since the waving of the lamellar interface is related to creep strain in one-to-one correspondence, the measurement of the broadening by X-ray diffraction can be utilized as a non-destructive method to predict the lifetime of Ni-base superalloys

## 6. Conclusion

The evolution of orientation distributions of  $\gamma$  and  $\gamma'$  phases in crept Ni-base single crystal superalloys, especially the waving of  $\gamma/\gamma'$  lamellar interface, has been investigated by theoretical calculations with elastic-plastic models and by experiments. The inclination of the lamellar interface affects significantly the internal stress states that determine the driving force for the motion of creep dislocations. The stress states with a non-tetragonal symmetry resulting from the inclination of lamellar interface cause the introduction of unequal numbers of dislocations for possible slip systems, which eventually results in the crystallographic rotation of the  $\gamma$  phase. The distribution of crystallographic rotations can be measured by X-ray diffractometry as a broadening of crystallographic orientation distributions resulting from various lamellar inclination angles different from place to place. Since the magnitude of the broadening of crystallographic orientation distributions directly related to the magnitude of creep strain, the measurement of the broadening by X-ray diffraction can be utilized in non-destructive methods to predict the lifetime of Ni-base superalloys.

## Acknowledgement

This work was supported by Grant-in-Aid for Scientific Research (B) from the Ministry of Education, Science, Sports and Culture of Japan and in part by the 21st Century COE (Center of Excellence) Program on United Approach for New Materials Science from MEXT, Japan.

## References

- [1] Tien JK, Gamble RP. Metall. Trans. 1972;3:2157.
- [2] Pearson DD, Lemkey FD, Kear BH. Superalloys 1980, The Minerals, Metals & Materials Society 1980:513.
- [3] Epishin A, Link T, Portella PD, Brückner U. Acta Mater. 2000;48:4169.
- [4] Tanaka K, Kajikawa T, Ichitsubo T, Osawa M, Yokokawa T, Harada H. Mater. Sci. Forum 2005;475-479:619.
- [5] Tanaka K, Ichitsubo T, Kishida K, Inui I, Matsubara E. Acta Mater. 2008;56:3786.
- [6] Kuhn HA, Biermann H, Ungár T, Mughrabi H. Acta Metall. Mater. 1991;39:2783.
- [7] Biermann H, Strehler M, Mughrabi H. Scripta Metall. Mater. 1995;32:1405.
- [8] Fährmann M, Wolf JG, Pollock TM. Mater. Sci. Eng. 1996;A210;8.
- [9] Royer A, Bastie P. Scripta Mater. 1997;36:1151.
- [10] Link T, Epishin A, Brückner U, Portella P. Acta Mater. 2000;48:1981.
- [11] Royer A, Jacques A, Bastie P, Véron M. Mater. Sci. Eng. 2001;A319-321;800.
- [12] Jacques A, Bastie P. Phil. Mag. 2003;83:3005.
- [13] Diologent F, Caron P, d'Almeida T, Jacques A, Bastie P. Nucl. Inst. Methods Phys. Res. 2003;B200;346.
- [14] Colonnetti G. Atti Accad. Naz Lincei Rc. 1915;24;404.
- [15] Mura T. Micromechanics of defects in solids. 2nd revised ed. The Hague: Martinus Nijhoff Publisher, 1987.
- [16] Ichitsubo T, Koumoto D, Hirao M, Tanaka K, Osawa M, Yokokawa T, Harada H. Acta Mater. 2003;51:4033.
- [17] Epishin A, Link T. Superalloys 2004, The Minerals, Metals & Materials Society 2004:137.

- [18] Müller L, Glatzel U, Feller-Kniepmeier M. *Acta Metall. Mater.* 1993;41:3401.
- [19] Pollock TM, Argon AS. *Acta Metall. Mater.* 1992;40:1.
- [20] Sass V, Feller-Kniepmeier M. *Mater. Sci. Eng.* 1998;A245:19.
- [21] Zhang JX, Murakumo T, Koizumi Y, Harada H. *J. Mater. Sci.* 2003;38:4883.
- [22] Wang YU, Jin YM, Cuitino AM, Khachaturyan AG. *Acta Mater.* 2001;49:1847.
- [23] Khachaturyan AG. *Theory of Structural Transformation in Solids*, (Wiley, New York, 1983).
- [24] Ichitsubo T, Koumoto D, Hirao M, Tanaka K, Osawa M, Yokokawa T, Harada H. *Acta Mater.* 2003;51:4863.
- [25] Inoue T, Tanaka K, Kishida K, Okamoto NL, Inui H, Yokokawa T, Harada H. to be published.

## Figure captions

Fig. 1. Two types of the models of the raft structure for internal stresses and elastic energy calculations. (a): wavy lamellar structure. (b): tilted lamellar structure.

Fig. 2. Experimental set-up of the instrument for measuring the rocking curve. X-ray is transmitted through a thin-plate specimen to avoid the effect of surface relaxation of elastic fields.

Fig. 3. Variation of the elastic energy of the wavy lamellar structure as a function of the maximum tilting angle of the wave.

Fig. 4. Elastic stress tensors with an external tensile stress of 137 MP at typical three different points in the wavy lamellar structure of the  $\gamma$  phase indicated in the illustration.

Fig. 5. Evolutions of amounts of creep dislocation belonging to different slip systems and the driving force calculated by the equations (7) for (a) and (b) and (7') for (c) and (d), respectively. (a)  $\theta = \varphi = 0$ , (b)  $\theta = 0$  and  $\varphi = 5^\circ$ , (c)  $\theta = 0$  and  $\varphi = 5^\circ$  and (d)  $\theta = 0$  and  $\varphi = 20^\circ$ .

Fig. 6. Deviation of crystallographic orientation determined by EDX-EBSD analysis. (a): Cr-EDX image. (b): crystallographic misorientation determined at the points along a line. (c): distribution of the crystallographic orientation of  $\gamma$  and  $\gamma'$  phases with respect to the averaged orientation, respectively.

Fig. 7. Evolutions of the full width of the half maximum (FWHM) of the rocking curve as a function of creep strain for the diffractions of 004, 400, 003 and 300.

Fig. 8. Schematic illustrations of crystallographic rotation. (a): without restriction from the  $\gamma'$  plate; plastically deformed  $\gamma$  phase by slips overlaps to the  $\gamma'$  phase and a void forms. (b): with restriction from the  $\gamma'$  plate lying on (001); overlapping and forming a void are canceled by a crystallographic rotation of the  $\gamma$  phase along the direction of the

line vector of interfacial dislocations.

Fig. 9. Schematic illustrations of the distribution of the crystallographic orientations caused by a rotating mechanism illustrated in Fig. 8. (a): Three-dimensional illustration of the distributions. The arrows labeled  $\omega$  are the scanning direction for measuring the rocking curve corresponding to the specimen rotation as illustrated in Fig. 2. The arrows labeled as  $\chi$  is the scanning direction adopted in an additional experiment (see text). (b) and (c): detail shape of the broadening of the  $[00l]$  and  $[hk0]$  poles, respectively. Note that the horizontal axis of (c) is magnified by 100 times with respect to the vertical axis.

Fig. 10. The rocking curves and the full width of the half maximum (FWHM) for (a) the 004 diffraction, and for 400 diffraction scanned along (b)  $\omega$  and (c)  $\chi$  direction, respectively.

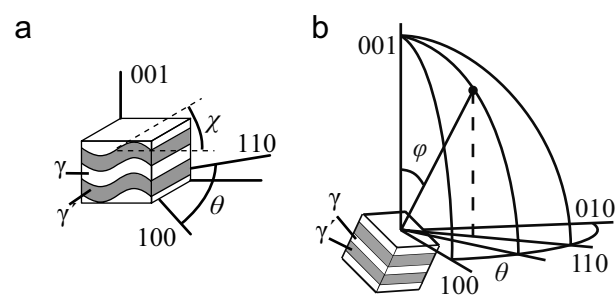


## Table captions

Table 1. Chemical composition (at.%) of the Ni-base superalloy of TMS-26.

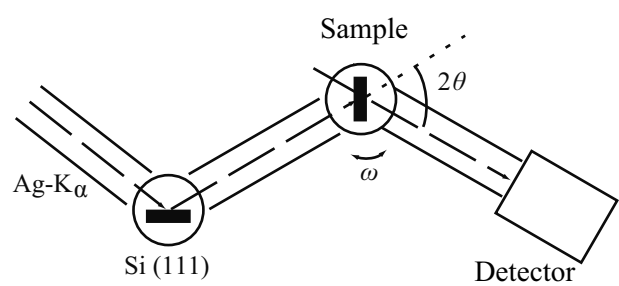
Table 2. The axis of crystallographic rotation and its direction of 8 of 12 slip systems with the Burgers vector of  $\frac{1}{2}\langle 101 \rangle$ .

Figure1



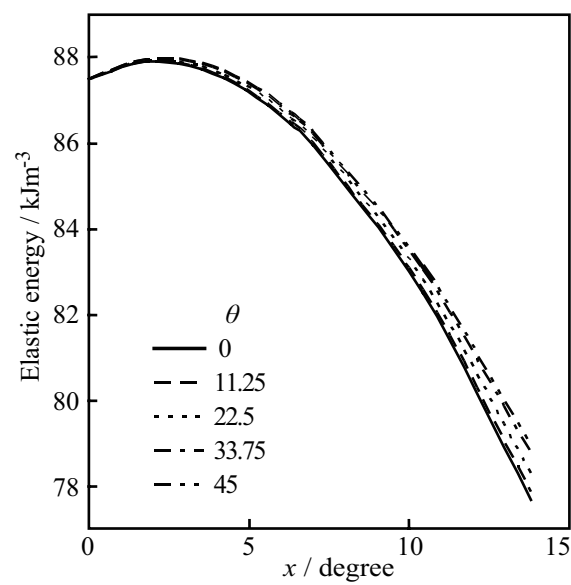
Inoue et al.  
Fig. 1

Figure2



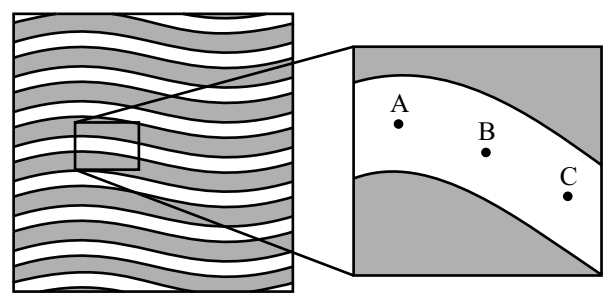
Inoue et al.  
Fig.2

Figure3



Inoue et al.  
Fig.3

Figure4

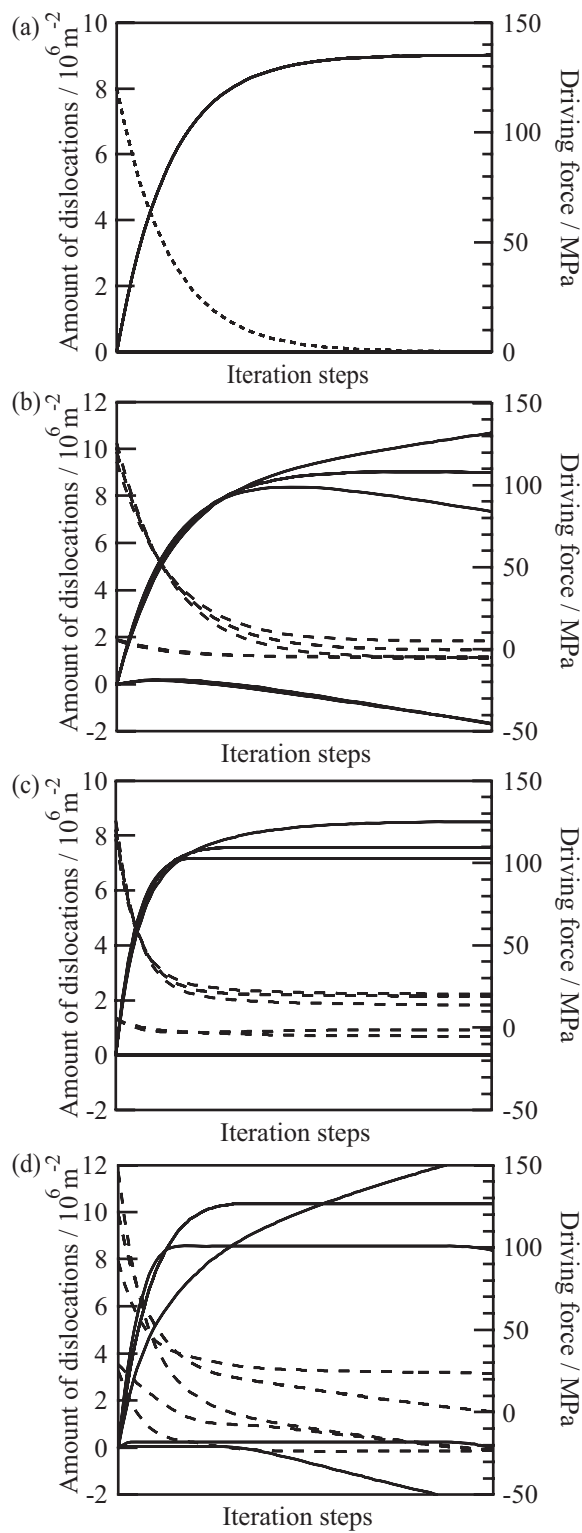


Elastic stresses / MPa

A	B	C
$\begin{pmatrix} 135 & -1 & 0 \\ -1 & 133 & 0 \\ 0 & 0 & 140 \end{pmatrix}$	$\begin{pmatrix} 129 & -3 & 1 \\ -3 & 115 & -19 \\ 1 & -19 & 139 \end{pmatrix}$	$\begin{pmatrix} 124 & -6 & 2 \\ -6 & 99 & -23 \\ 2 & -23 & 141 \end{pmatrix}$

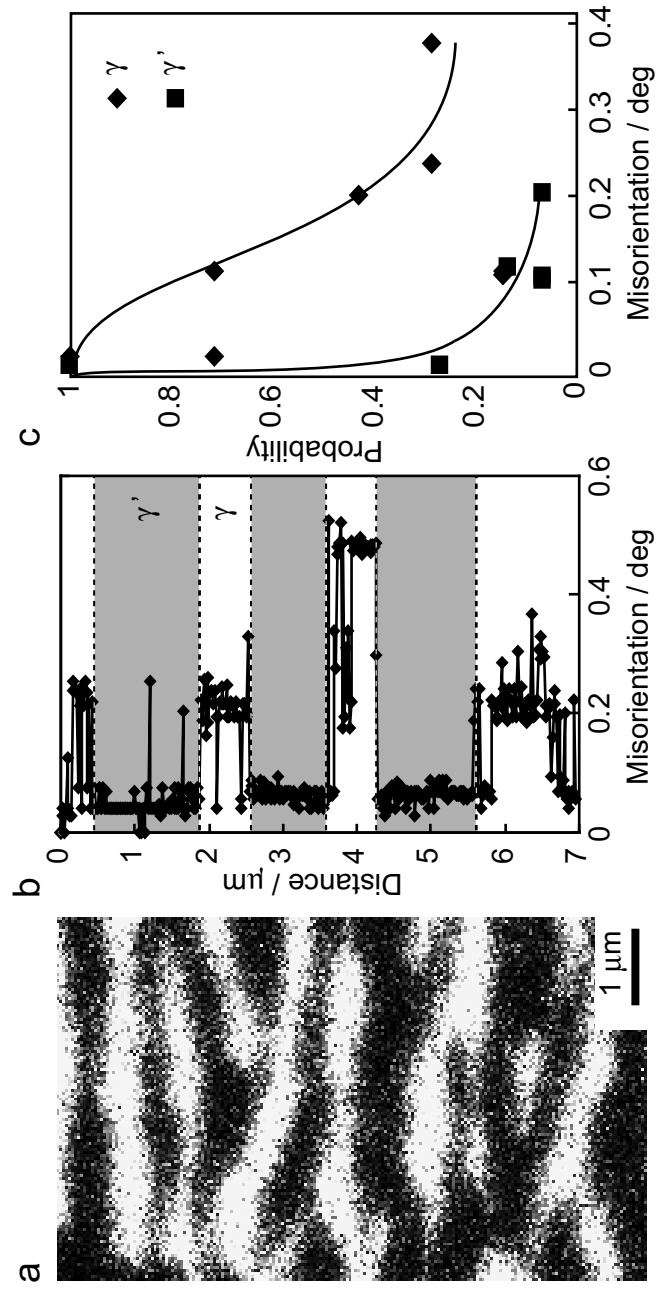
Inoue et al.  
Fig.4

Figure5



Inoue et al.  
Fig.5

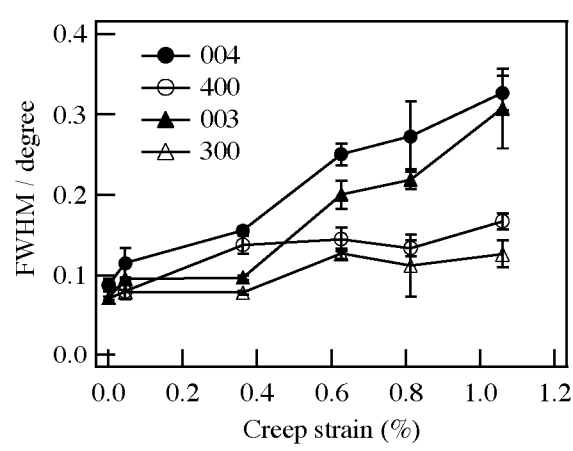
Figure6



Inoue et al.

Fig.6

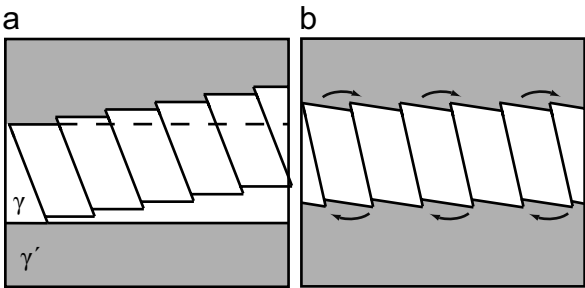
Figure7



Inoue et al.  
Fig.7

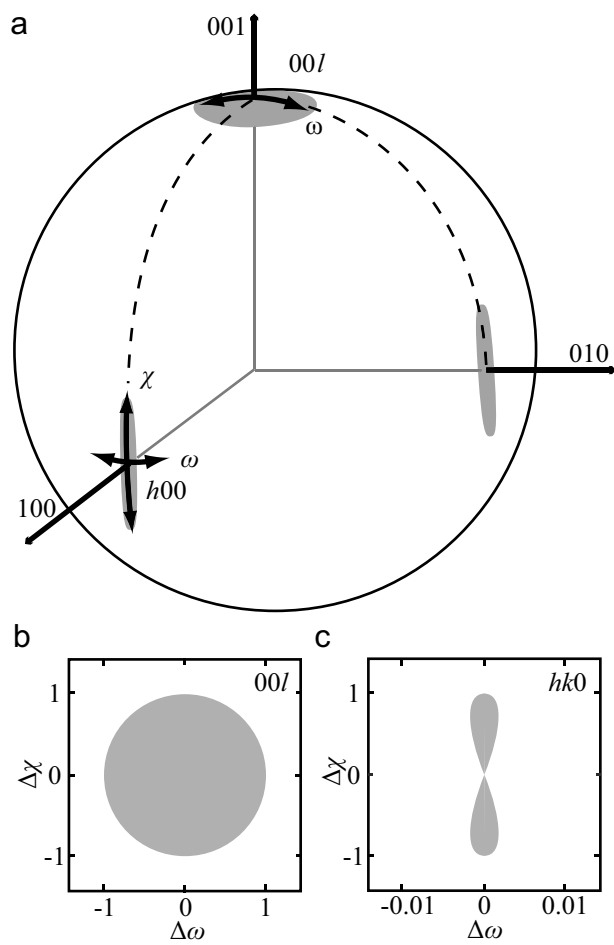


Figure8



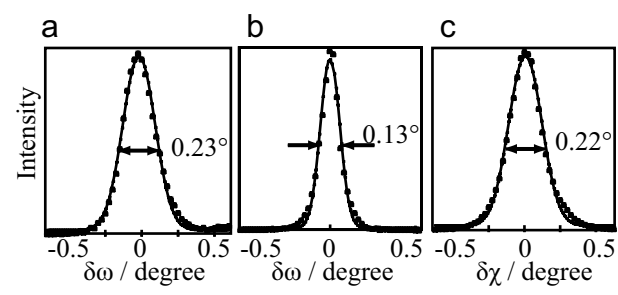
Inoue et al.  
Fig.8

Figure9



Inoue et al.  
Fig.9

Figure10



Inoue et al.  
Fig.10

Table 1. Chemical composition (at.%) of the Ni-base superalloy of TMS-26.

Nominal	Ni	Co	Cr	Mo	W	Al	Ta
at. %	64.8	8.82	6.34	1.26	3.97	11.98	2.84

Table 2. The axis of crystallographic rotation and its direction of 8 of 12 slip systems with the Burgers vector of  $1/2\langle 101 \rangle$ .

$i$	Slip system	Axis of rotation	Direction of the rotation
1	$[101](\bar{1}\bar{1}1)$	$[1\bar{1}0]$	+
2	$[101](\bar{1}11)$	$[110]$	-
3	$[\bar{1}01](111)$	$[1\bar{1}0]$	-
4	$[\bar{1}01](1\bar{1}1)$	$[110]$	+
5	$[011](\bar{1}\bar{1}1)$	$[1\bar{1}0]$	+
6	$[011](1\bar{1}1)$	$[110]$	+
7	$[0\bar{1}1](111)$	$[1\bar{1}0]$	-
8	$[0\bar{1}1](\bar{1}11)$	$[110]$	-